

Precisely designing asymmetrical selenium-based dual-atom sites for efficient oxygen reduction

Received: 29 May 2024

Accepted: 2 January 2025

Published online: 07 January 2025

Check for updates

Xiaochen Wang^{1,5}, Ning Zhang^{2,5}, Huishan Shang¹✉, Haojie Duan³, Zhiyi Sun⁴, Lili Zhang¹, Yuanting Lei¹, Xuan Luo³✉, Liang Zhang³, Bing Zhang¹ & Wenxing Chen⁴✉

Owing to their synergistic interactions, dual-atom catalysts (DACs) with well-defined active sites are attracting increasing attention. However, more experimental research and theoretical investigations are needed to further construct explicit dual-atom sites and understand the synergy that facilitates multistep catalytic reactions. Herein, we precisely design a series of asymmetric selenium-based dual-atom catalysts that comprise heteronuclear $\text{SeN}_2\text{-MN}_2$ ($\text{M} = \text{Fe}, \text{Mn}, \text{Co}, \text{Ni}, \text{Cu}, \text{Mo}, \text{etc.}$) active sites for the efficient oxygen reduction reaction (ORR). Spectroscopic characterisation and theoretical calculations revealed that heteronuclear selenium atoms can efficiently polarise the charge distribution of other metal atoms through short-range regulation. In addition, compared with the Se or Fe single-atom sites, the SeFe dual-atom sites facilitate a reduction in the conversion energy barrier from $^*\text{O}$ to $^*\text{OH}$ via the coadsorption of $^*\text{O}$ intermediates. Among these designed selenium-based dual-atom catalysts, selenium-iron dual-atom catalysts achieves superior alkaline ORR performance, with a half-wave potential of 0.926 V vs. a reversible hydrogen electrode. In addition, the $\text{SeN}_2\text{-FeN}_2$ -based Zn-air battery has a high specific capacity (764.8 mAh g^{-1}) and a maximum power density (287.2 mW cm^{-2}). This work may provide a good perspective for designing heteronuclear DACs to improve ORR efficiency.

The increase in the next generation of renewable energy storage and conversion technologies, such as metal-air batteries and fuel cells, is projected to minimise the dependency on fossil fuels and achieve net zero emissions¹⁻⁶. However, their commercial application has been severely restricted by the irreplaceable cathodic oxygen reduction reaction (ORR), which has sluggish kinetics⁷. This restriction has motivated the development of platinum-free ORR electrocatalysts with high performance, affordable costs, and high durability⁸⁻¹⁰. Recently,

the use of metal-nitrogen-carbon single-atom catalysts (SACs) has fostered a fresh research surge because of their high atom utilisation efficiency and alterable electronic structure¹¹⁻¹⁶. Among the frequently studied transition metal-based SACs, Fe-N-C is the most active leading candidate and is promising as a substitute for commercial Pt/C catalysts¹⁷⁻¹⁹. However, SACs have difficulty efficiently driving multiple elementary catalytic reactions and disrupting the linear connection between the adsorption energies of intermediates²⁰⁻²⁴. Compared with

¹School of Chemical Engineering, Zhengzhou University, Zhengzhou, P. R. China. ²Zhongyuan Critical Metals Laboratory, Zhengzhou University, Zhengzhou, P. R. China. ³Centre for Combustion Energy, School of Vehicle and Mobility, State Key Laboratory of Intelligent Green Vehicle and Mobility, Tsinghua University, Beijing, P. R. China. ⁴Energy & Catalysis Centre, School of Materials Science and Engineering, Beijing Institute of Technology, Beijing, China. ⁵These authors contributed equally: Xiaochen Wang, Ning Zhang. ✉e-mail: shanghs@zzu.edu.cn; lx1107@mail.tsinghua.edu.cn; wxcchen@bit.edu.cn

conventional M–N₄ active sites, asymmetry-coordinated M–N–C SACs (with asymmetric configurations such as M–N_x, M–N_x–P/S/B/O/Cl/I and M–M) can tailor the interaction between active sites and intermediates because of the unique electron-filling state and asymmetric charge distribution of central metal atoms²⁵. The inherent catalytic activity of Fe–N–C for the ORR is highly related to the electronic states of the active sites, which can be tailored through asymmetric coordinated engineering²⁶. An asymmetrically coordinated M–M configuration involves the introduction of a second metal atom adjoining one metal centre to construct dual-metal atomic sites²⁷. These asymmetric M–M dual-atom catalysts inherit the advantages of maximal atomic utilisation and adjustable coordination configurations for SACs while providing the opportunity to increase the catalytic efficiency by exploiting synergistic effects^{28,29}. The electronic structure of asymmetrically coordinated adjoining two-metal atoms can potentially be adjusted by their interaction, which in turn refines the adsorption/desorption of intermediates towards the top of the activity volcano plot^{30,31}. Currently, some transition metals have been successfully introduced to construct dual-metal atomic pairs (Fe–Co³², Fe–Ni³³, Fe–Cu³⁴, Fe–Zn³⁵, Fe–Mn³⁶, and Fe–Mo³⁷), simultaneously triggering charge redistribution and offering asymmetric sites to reduce the reaction energy barriers.

In addition to constructing dual-metal active sites, incorporating nonmetallic atoms can not only tune the *d*-band centre of the central metal³⁸ but also offer additional synergistic sites to facilitate the conversion of ORR intermediates. For example, Zong et al.³⁹ devised Fe, P dual-atom sites to disrupt conventional scaling relationships via second-sphere hydrogen bonding interactions, which favour the adsorption/desorption of oxygen-containing species and accelerate the reaction kinetics of the ORR⁴⁰. Recently, Sun et al.⁴¹ constructed an asymmetrical Cu–Se dual-atom catalyst, in which the Se₁–C₂ moiety can function as a synergistic site to accelerate the transformation from OOH*(Cu₁–N₄) to O*(Se₁–C₂). The selenium (Se) atom (4s² 4p⁴), a chalcogen element, possesses more valence electrons than the C (2s² 2p²) and N (2s² 2p³) atoms do, which is expected to tailor the electron structure of the central metal atom more efficiently^{42–44}.

Herein, various asymmetric SeM–C₂N (M = Fe, Mn, Co, Ni, Cu, Mo, etc.) dual-atom catalysts comprising SeN₂–MN₂ active sites were successfully synthesised via a three-step pyrolysis strategy. The obtained SeM–C₂N dual-atom catalysts both achieve satisfactory alkaline ORR activity. SeFe–C₂N exhibited the highest half-wave potential of 0.926 V vs. RHE. The Se modulator can regulate the local coordination configuration and the electronic structure of central Fe sites by triggering a polarised charge distribution. More importantly, the codoping of Se and Fe atoms appropriately facilitates the transformation of *O to *OH, which considerably increases the four-electron ORR activity. Consequently, the SeFe–C₂N catalyst achieves a remarkable maximum power density of 287.2 mW cm^{−2} and noteworthy sustainability for up to 380 h in an alkaline Zn–air battery.

Results

Synthesis and characterisation of SeFe–C₂N

Figure 1a schematically illustrates the fabrication approach for SeFe–C₂N. First, the cross-linked polymer was synthesized by heating the mixture of cyclohexanehexone and urea at 90 °C (Supplementary Figs. 1–2). This initial preorganisation of precursors leads to the formation of a stable aromatic skeletal structure (Supplementary Figs. 3–5 and Table 1), which would not experience substantial rearrangement during subsequent pyrolysis treatment. Following a salt melt synthesis process with anhydrous MgCl₂ at 900 °C, a C₂N material with a high relative content of pyrrolic or pyrazine-like nitrogen species was obtained (Supplementary Fig. 6). Moreover, sufficient acid leaching and water/ethanol washing were conducted to eliminate potential Mg-containing residues (Supplementary Figs. 7–9 and Table 2), thereby facilitating the successive, precise synthesis of the target catalyst. The resulting C₂N substrate is characterised by a well-defined micropore

structure (N₆ cavities), which is tightly covered by pyrazine-like nitrogen and has a high degree of similarity to the ideal C₂N^{45–47}.

Notably, the unsaturated *sp*²-bonded edge N in the N₆ cavities can serve as promising coordination sites to anchor metal atoms^{48–51}. The obtained C₂N substrate was subsequently mixed with SeO₂ at a weight ratio of 1:1 by grinding, after which it was subjected to a second round of pyrolysis at 1000 °C under a N₂ atmosphere to synthesize Se–C₂N. After absorbing the Fe³⁺ precursors and performing a third pyrolysis treatment at 900 °C under a N₂ atmosphere, the SeFe–C₂N sample with the asymmetrically coordinated dual atom sites immobilised on the two-dimensional C₂N was obtained. For comparison, the Se–C₂N and Fe–C₂N samples were fabricated via a similar process.

Transmission electron microscopy (TEM) demonstrated that SeFe–C₂N possesses a two-dimensional nanosheet structure (Fig. 1b). There is no detectable metal or metallic oxide, which is consistent with the powder X-ray diffraction (PXRD) patterns (Supplementary Fig. 10), indicating the atomically dispersed state of Se and Fe atoms. Additionally, the element mapping in Fig. 1c reveals that Se, Fe, N, and C are homogeneously scattered throughout the sample. As shown in Supplementary Figs. 11–12, Se–C₂N and Fe–C₂N exhibit similar morphologies and atomic element distributions. Aberration-corrected high-angle annular dark-field scanning TEM (HAADF-STEM) can identify the atomically dispersed state of a metal in more detail. On the one hand, the distance between two adjacent metal atoms can be determined from HAADF-STEM images. In contrast to single-atom sites, the interatomic distance between adjacent metal atoms in dual-atom sites supported on nitrogen-doped carbon materials is typically narrowed within the range of the fourth coordination shell (M1–M2 distance ≤ 5.3 Å). This proximity can lead to a considerable synergistic effect that alters the electronic structure and enhances the adsorption and desorption of intermediates⁵². On the other hand, the proportion of dual-atom sites within a microcosmic region, as derived from statistical analysis, can serve as an indicator of the overall percentage of dual-atom sites in the catalyst, thereby influencing the catalytic performance of the materials.

As illustrated in Fig. 1d, the atomic scattering of Se and Fe was further confirmed by the lack of Se or Fe nanoparticles. Importantly, most dual-atom sites (circled by yellow ellipses) and a few single-atom sites (marked by blue circles) are visible, which highlights the conjecture regarding an atypically active site. Supplementary Fig. 13 displays the evaluation of the ratio between dual-atom and single-atom sites. Dual-atom sites account for ~82% of the dominant active sites in SeFe–C₂N. Upon further magnification, the distance between neighbouring Se and Fe atoms is ~2.3 Å, which aligns with the pore spacing of the atoms and C₂N (Fig. 1e–f). This alignment suggests the stable existence of dual-atom Se–Fe sites. The intensity distribution (Fig. 1g) along the white dotted line reveals that the spacing between adjoining Se and Fe atoms was ~0.22 nm, which closely matches the effective diameter of Se/Fe atoms for interaction with each other. Moreover, some dot pairs were detected to be close quarters, which might be attributed to the abundant wrinkles and ripples in the C₂N matrix that prevent the coaxial line of Se–Fe pairs from being parallel to the basal plane, resulting in variable distances between the Se–Fe bimetal sites in the AC-STEM images. Supplementary Fig. 14 exclusively illustrates the Se–Fe distances from areas #2 to #4 in Fig. 1d and presents intuitive schematic models of Se–Fe bimetal sites immobilised on the C₂N framework. The results indicated that the visual distances of the Se–Fe sites were 0.26 nm, 0.23 nm, and 0.13 nm, respectively, which did not exactly correspond to the theoretical bond length of Se–Fe coordination. The different visual distances are due mainly to the axial rotation of the Se–Fe sites on the folded substrate. Typically, the visual distances of the Se–Fe bonds at axial distance rotations of 90°, 60°, and 30° are different. The contents of Se and Fe determined via inductively coupled plasma–optical emission spectrometry (ICP–OES) are 1.66 and

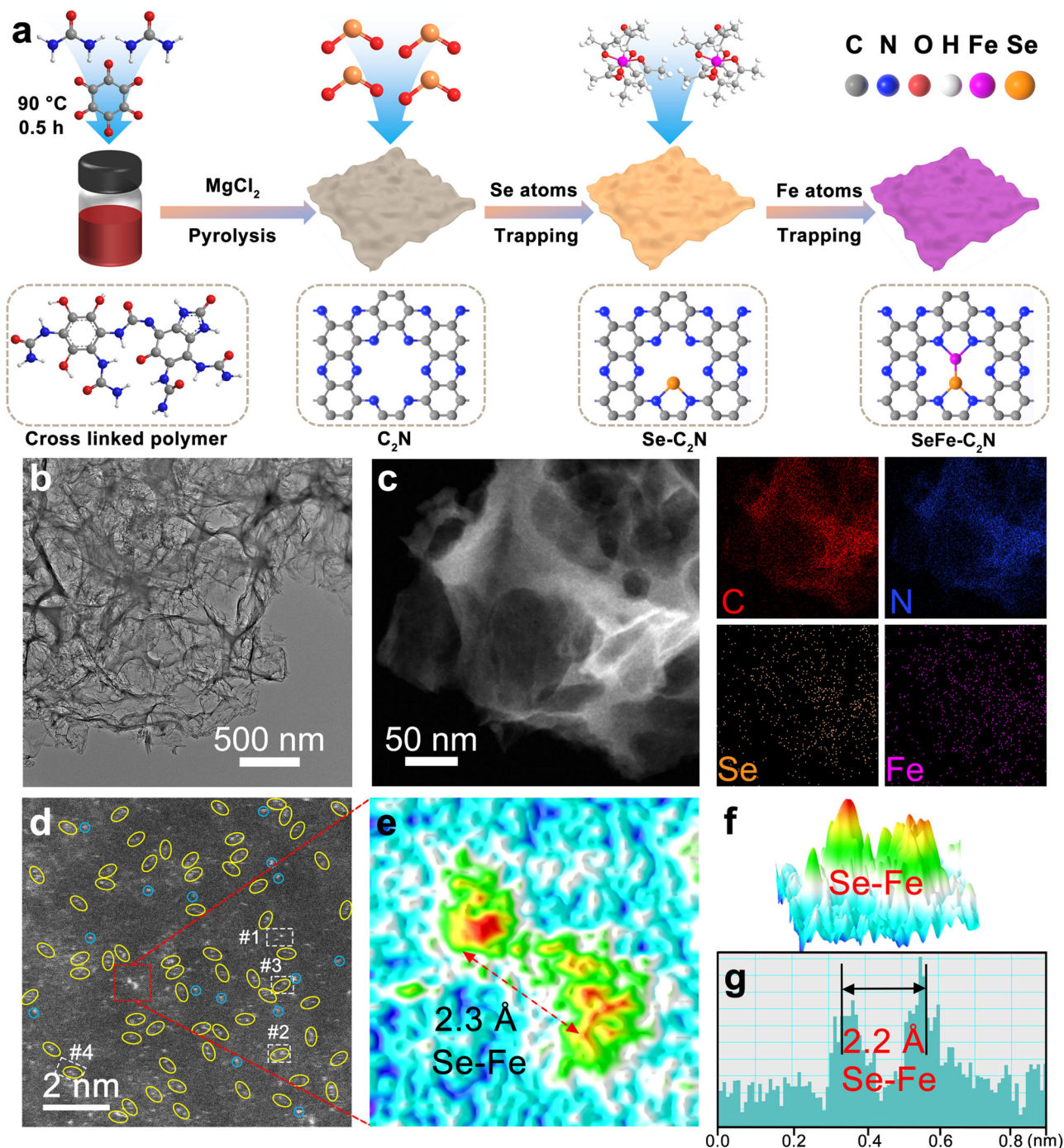


Fig. 1 | Morphology characterisation of SeFe-C₂N. **a** Illustration of the fabrication of SeFe-C₂N. **b** TEM image of SeFe-C₂N. **c** STEM image and elemental mapping of SeFe-C₂N. **d** HAADF-STEM image of SeFe-C₂N, showing the dual atoms (yellow

ellipse) dispersed in the C₂N substrate. **e** Intensity profiles highlighted along the red dotted line in **d**. **f** 3D model of dual-atom Se-Fe bright spots along the red dotted line and **g** corresponding intensity profiles around location #1 in **d**.

1.16 wt%, respectively, with a molar ratio of 1.01:1 (Supplementary Table 3).

The degree of graphitisation of SeFe-C₂N was analysed via Raman spectroscopy (Supplementary Fig. 15). In all the samples, only two characteristic peaks of carbon at 1372.6 cm⁻¹ (D band, disordered/defective carbon) and 1594.5 cm⁻¹ (G band, graphitic carbon) were detected. The intensity ratio (I_D/I_G) of the D band to the G band is an indicator used to evaluate the lattice distortion and crystallinity of the nanoarchitectures. Compared with those of C₂N (1.03), Se-C₂N (1.01), and Fe-C₂N (0.98), the I_D/I_G value of SeFe-C₂N decreases to 0.94, indicating that a greater degree of graphitisation is generated by three-

step pyrolysis, which is advantageous for electron transfer and the stability of the active site during the ORR⁵³. The N₂ adsorption-desorption measurements reveal that all samples display a typical type-I adsorption isotherm (Supplementary Fig. 16a), additionally revealing the existence of abundant micropores and small mesopores inherited from C₂N, which are generated during the high-temperature evaporation of MgCl₂ and conducive to active site exposure and mass transport during the ORR. With the immobility of Se/Fe on N₆ cavities, the surface area of the samples tends to decrease, and the microporous peak shifts negatively (Supplementary Figs. 16b-e). Additionally, the SeFe-C₂N catalyst has a slightly lower surface area (964.8 m²

g^{-1}) than $\text{Se-C}_2\text{N}$ ($1003.6 \text{ m}^2 \text{ g}^{-1}$) and $\text{Fe-C}_2\text{N}$ ($990.3 \text{ m}^2 \text{ g}^{-1}$), which results from the high occupation degree of Se/Fe dual sites within the micropores (N_6 cavities).

The surface elemental bonding information of $\text{SeFe-C}_2\text{N}$ was studied via X-ray photoelectron spectroscopy (XPS). The high-resolution C 1s spectra (Supplementary Fig. 17) of $\text{SeFe-C}_2\text{N}$ can be resolved into four peaks, which are associated with C=C, C-N/C=N, C-C, and carbon coordinated with doped Se (C-Se, 289.9 eV)^{54,55}. As depicted in Supplementary Fig. 18, the characteristic peak at 665.6 cm^{-1} corresponding to the Se-N bond was present in $\text{SeFe-C}_2\text{N}$ and $\text{SeFe-C}_2\text{N}$. This peak confirmed the existence of Se-N in $\text{SeFe-C}_2\text{N}$ and $\text{SeFe-C}_2\text{N}$ ⁵⁶. According to Supplementary Fig. 19, metal-N species appear in $\text{Se-C}_2\text{N}$, $\text{Fe-C}_2\text{N}$, and $\text{SeFe-C}_2\text{N}$, demonstrating the coordination of atomically dispersed Se and Fe atoms with N atoms. Then, the electron transitions of Se, Fe, and N are determined from the XPS spectrum. Compared with those of $\text{Fe-C}_2\text{N}$ and $\text{Se-C}_2\text{N}$, the N 1s binding energies of $\text{SeFe-C}_2\text{N}$ shift to higher energy positions by 0.2 eV and 0.1 eV, respectively. This comparison indicates the existence of an electron-poor state of N atoms around Fe and Se. In addition, the characteristic Se 3d peak of Se-N shifts negligibly (-0.1 eV) after the introduction of Fe atoms into $\text{Se-C}_2\text{N}$, which suggests that the Se atom becomes slightly electron rich (Supplementary Fig. 20). Apparently, a new peak located at 49.8 eV appears in the high-resolution Se 3d XPS spectrum of $\text{SeFe-C}_2\text{N}$, which might be attributed to Se-Fe interactions. Compared with that of $\text{Fe-C}_2\text{N}$, the Fe $2p_{1/2}$ peak in $\text{SeFe-C}_2\text{N}$ shifted towards a lower bonding energy position (-0.5 eV), indicating a considerable transfer of electrons to the Fe atom (Supplementary Fig. 21). Above all, after the Fe and Se atoms form orbital interactions, electron transfer occurs from the N atoms to the coordinated Fe and Se atoms, resulting in a large change in the Fe oxidation state and a slight change in the Se oxidation state.

The valence states and atomic coordinated configurations of the Se and Fe atoms in the $\text{SeFe-C}_2\text{N}$ catalyst were examined via X-ray absorption spectroscopy (XAS). As shown by the Se K-edge X-ray absorption near-edge structure (XANES) spectra (Fig. 2a), the adsorption threshold positions of $\text{Se-C}_2\text{N}$ and $\text{SeFe-C}_2\text{N}$ are higher than that of Se foil but lower than that of SeO_2 , implying the positive valence of Se. The oxidation state of the transition metal can be obtained by fitting the position of the absorption edge of the metal linearly. The metal absorption edge was located using the maximal value of the first derivative of XANES. As shown in Supplementary Fig. 22, the first-derivative Se K-edge XANES curve for $\text{SeFe-C}_2\text{N}$ is comparable to that of $\text{Se-C}_2\text{N}$, revealing the slightly decreased oxidation state of Se in $\text{SeFe-C}_2\text{N}$ compared with $\text{Se-C}_2\text{N}$. Furthermore, the Fourier transformed k^3 -weighted extended X-ray absorption fine structure (FT-EXAFS) spectrum of $\text{SeFe-C}_2\text{N}$ exhibited one major peak and small peaks at 1.48 Å and 2.28 Å in R space, reflecting the Se-N and Se-Fe first coordination shells, respectively (Fig. 2b). Compared with that of Se foil, the Se-Se coordination peak (2.08 Å) is absent in $\text{Se-C}_2\text{N}$ and $\text{SeFe-C}_2\text{N}$, demonstrating the atomically dispersed state of the Se atom. Similarly, the adsorption threshold position of the Fe K-edge for $\text{SeFe-C}_2\text{N}$ is located between those of the Fe foil and Fe_2O_3 (Fig. 2c), which indicates a positive valence state ($+0 < \delta < +3$) of Fe. Similarly, the fitted Fe oxidation state of the $\text{SeFe-C}_2\text{N}$ sample from the Fe K-edge XANES spectra is lower than that of $\text{Fe-C}_2\text{N}$ (Supplementary Fig. 23), which aligns with the Fe 2p XPS results (Supplementary Fig. 21). The lower oxidation states of Fe and Se in $\text{SeFe-C}_2\text{N}$ than in $\text{Fe-C}_2\text{N}$ and $\text{Se-C}_2\text{N}$ contributed to the polarised charge redistribution through Se-Fe electronic interactions. In addition, the different small preedges at -7110 eV for $\text{SeFe-C}_2\text{N}$ and $\text{Fe-C}_2\text{N}$ are generally assigned to the $1s \rightarrow 3d$ transition. Additionally, as shown in Fig. 2a and Fig. 2c, the left-shift phenomenon is monitored at the Se K-edge and the Fe K-edge, but owing to the unique semimetallic feature of selenium, the absorption threshold shift is smaller than that of iron in the asymmetrical $\text{SeN}_2\text{-FeN}_2$ system, which is also influenced by adjacent nitrogen

and carbon atoms. The electron redistribution Fe active site is advantageous for triggering the adsorption of oxygen molecules⁵⁷.

As shown in Fig. 2d, the Fe K-edge FT-EXAFS spectrum of $\text{SeFe-C}_2\text{N}$ presents an apparent peak at -1.50 Å and a shoulder peak at -2.28 Å , which are ascribed to the presence of Fe-N and Fe-Se coordination, respectively. Furthermore, the origin of the backscattering paths for $\text{SeFe-C}_2\text{N}$ is displayed in Supplementary Fig. 24. The Fe-N and Fe-Se scattering paths fit well with the $\text{SeFe-C}_2\text{N}$ at the Fe K-edge. Moreover, the $\text{SeFe-C}_2\text{N}$ at the Se K-edge matches well with the Se-N and Se-Fe bonds, demonstrating the existence of Fe-N, Se-N, and Se-Fe bonds in $\text{SeFe-C}_2\text{N}$. To further identify the fine coordination configurations of Se and Fe for different samples, quantitative least squares EXAFS curve-fitting analyses were conducted (Fig. 2e and Supplementary Figs. 25–27). Herein, the origin of the backscattering paths (Fe-N, Fe-Se, Se-N, and Se-Fe) used in the EXAFS fitting is based on FEFF calculations through the preset atomic model ($\text{SeN}_2\text{-FeN}_2$ moiety)⁵⁸. The fitting results of $\text{SeFe-C}_2\text{N}$ (Supplementary Table 4) reveal that the Se atom is coordinated with two nitrogen atoms (bond length of 1.85 Å) and one iron atom (bond length of 2.56 Å). Analogously, the average coordination numbers of N and Se around the Fe atom in $\text{SeFe-C}_2\text{N}$ are 2.1 (bond length of 2.01 Å) and 0.9 (bond length of 2.54 Å), respectively (Supplementary Table 5). The local structural parameters of $\text{SeFe-C}_2\text{N}$ indicate that Se/Fe atoms are coordinated as asymmetric dual-atom $\text{SeN}_2\text{-FeN}_2$ interface sites on the C_2N matrix.

On the basis of the XAS results, a three-dimensional atomic interface structure model of $\text{SeFe-C}_2\text{N}$ was constructed, as shown in Fig. 2f. To investigate the asymmetrical $\text{SeN}_2\text{-FeN}_2$ dual-atom sites in depth, the theoretical XANES spectrum was also calculated on the basis of the $\text{SeN}_2\text{-FeN}_2$ model at the Se K-edge and Fe K-edge (Supplementary Figs. 28–29). We found that the calculation curves for $\text{SeN}_2\text{-FeN}_2$ could effectively reproduce the main features of the experimental spectra of $\text{SeFe-C}_2\text{N}$. In addition, wavelet transform (WT) analysis was conducted to further distinguish the backscattering atoms. The WT contour plots of $\text{SeFe-C}_2\text{N}$ at the Se K-edge (Fig. 2g) and Fe K-edge (Fig. 2h) exhibit a predominant intensity maximum at 5.5 Å^{-1} , attributed to the Se/Fe-N interaction, and a second intensity maximum at 6.2 Å^{-1} , corresponding to Se-Fe coordination. In contrast to the contour plots of the Se foil and Fe foil, no identifiable Se-Se or Fe-Fe signals are observed. Collectively, the Se and Fe species were shown to be atomically distributed in $\text{SeFe-C}_2\text{N}$ with an asymmetric dual-atom $\text{SeN}_2\text{-FeN}_2$ coordination structure.

Electrocatalytic ORR performance

The ORR activities of the $\text{SeM-C}_2\text{N}$ catalysts were measured in an O_2 -saturated 0.1 M alkaline electrolyte via a catalyst-modified rotating disk electrode (Supplementary Fig. 30). The cyclic voltammograms (CVs) recorded in an O_2 atmosphere show obvious cathodic peaks, implying a certain ORR performance for all the samples (Fig. 3a)⁵⁹. As demonstrated by the linear sweep voltammetry (LSV) curves, the $\text{SeFe-C}_2\text{N}$ catalyst exhibited optimum activity, with a higher half-wave potential ($E_{1/2}$) of 0.926 V vs. RHE and the most positive onset (E_{onset}) of 1.06 V (Fig. 3b, c). Moreover, the $\text{Se-C}_2\text{N}$ and $\text{Fe-C}_2\text{N}$ catalysts display considerably lower $E_{1/2}$ values of 0.859 and 0.867 V, respectively, suggesting the synergistic effect of Se/Fe cooperation on increasing ORR catalysis. To further validate the superiority of the $\text{SeFe-C}_2\text{N}$ catalyst, a comparative analysis was conducted on various platinum mass loadings in Pt/C. As illustrated in Supplementary Fig. 31, the optimal $E_{1/2}$ of the Pt/C-modified working electrodes, with differing platinum mass loadings, reached a maximum of 0.888 V, which is 38 mV lower than that of the $\text{SeFe-C}_2\text{N}$ catalyst. Additionally, Fe/C materials with varying Fe loadings were synthesised, as shown in Supplementary Fig. 32. The ORR performance of these Fe/C materials is presented in Supplementary Fig. 33. These findings indicate that the Fe/C materials exhibited low alkaline ORR activities, which are considerably inferior to those of the $\text{SeFe-C}_2\text{N}$ catalyst. In addition, the number of pyrolysis

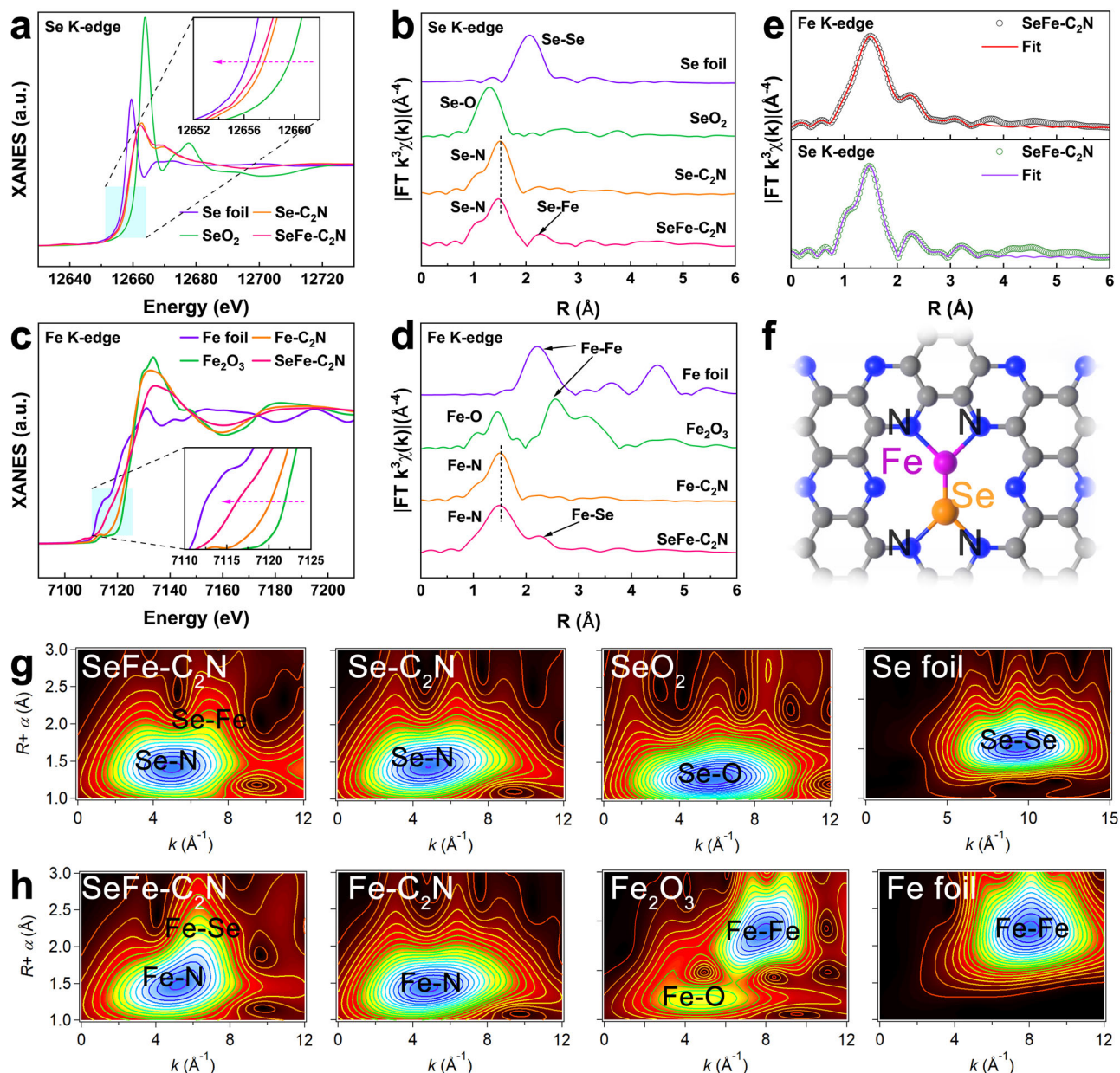


Fig. 2 | Atomic local structure characterisation of SeFe-C₂N. **a** Normalised Se K-edge XANES spectra and corresponding **b** FT k^3 -weighted EXAFS spectra of SeFe-C₂N. **c** Normalised Fe K-edge XANES spectra and matching **d** FT of k^3 -weighted EXAFS spectra of SeFe-C₂N. **e** FT-EXAFS fitting curve in R space of SeFe-C₂N at the

Se and Fe K-edges. **f** Structural model of the active site (SeN₂-FeN₂) derived from the EXAFS result. **g, h** WT for the FT k^3 -weighted $\chi(k)$ -function of SeFe-C₂N and reference samples at the Se and Fe K-edges, respectively.

steps may result in varying levels of activity between the SeFe-C₂N group and the other control groups. Accordingly, additional control groups of the catalysts, including the Se-C₂N-2nd and Fe-C₂N-2nd catalysts, have been included (Supplementary Figs. 34–36). Despite comparable degrees of graphitisation, the ORR activities of the Se-C₂N-2nd ($E_{1/2} = 0.906$ V) and Fe-C₂N-2nd ($E_{1/2} = 0.858$ V) catalysts were lower than that of the SeFe-C₂N ($E_{1/2} = 0.926$ V) catalyst (Supplementary Figs. 37–38). This comparison further substantiates the assertion that the superior catalytic performance of SeFe-C₂N is attributed to the synergistic effect of the Se-Fe dual-atom sites. Additionally, the kinetic current density (j_k) of SeFe-C₂N at 0.9 V reaches 13.3 mA cm⁻², which is 5.5 times greater than that of Se-C₂N (2.4 mA cm⁻²), 5.1 times greater than that of Fe-C₂N (2.6 mA cm⁻²), and 8.3 times greater than that of Pt/C (1.6 mA cm⁻², Fig. 3c). Furthermore, the value of the Tafel slope (Fig. 3d) for SeFe-C₂N (72.0 mV dec⁻¹) is lower than those of the Se-C₂N (114.6 mV dec⁻¹), Fe-C₂N (98.0 mV dec⁻¹), and Pt/C (100.9 mV

dec⁻¹) catalysts, demonstrating that SeFe-C₂N requires a smaller overpotential to achieve the same current density. Therefore, the smaller Tafel slope of the SeFe dual-atom sites suggests strengthened ORR kinetics^{27,60}.

In addition, LSV curves rotating at various rates (400–2500 rpm, Fig. 3e) were obtained to test the ORR pathways of SeFe-C₂N. The corresponding fitted Koutechy–Levich (K–L) plots (Fig. 3f) show that SeFe-C₂N exhibits first-order reaction kinetics with respect to the oxygen concentration. Over the whole potential range, the electron transfer number (n) is estimated to be in the range of 3.97–4.05. As illustrated in Fig. 3g, the rotating ring disk electrode (RRDE) measurement results in a low H₂O₂ yield of less than 4%, which further suggests the direct 4e⁻ ORR pathway on the catalyst. Nyquist plots of electrochemical impedance spectroscopy (EIS) were employed to evaluate the charge transfer properties of all the catalysts. As illustrated in Supplementary Fig. 39, SeFe-C₂N delivers the smallest

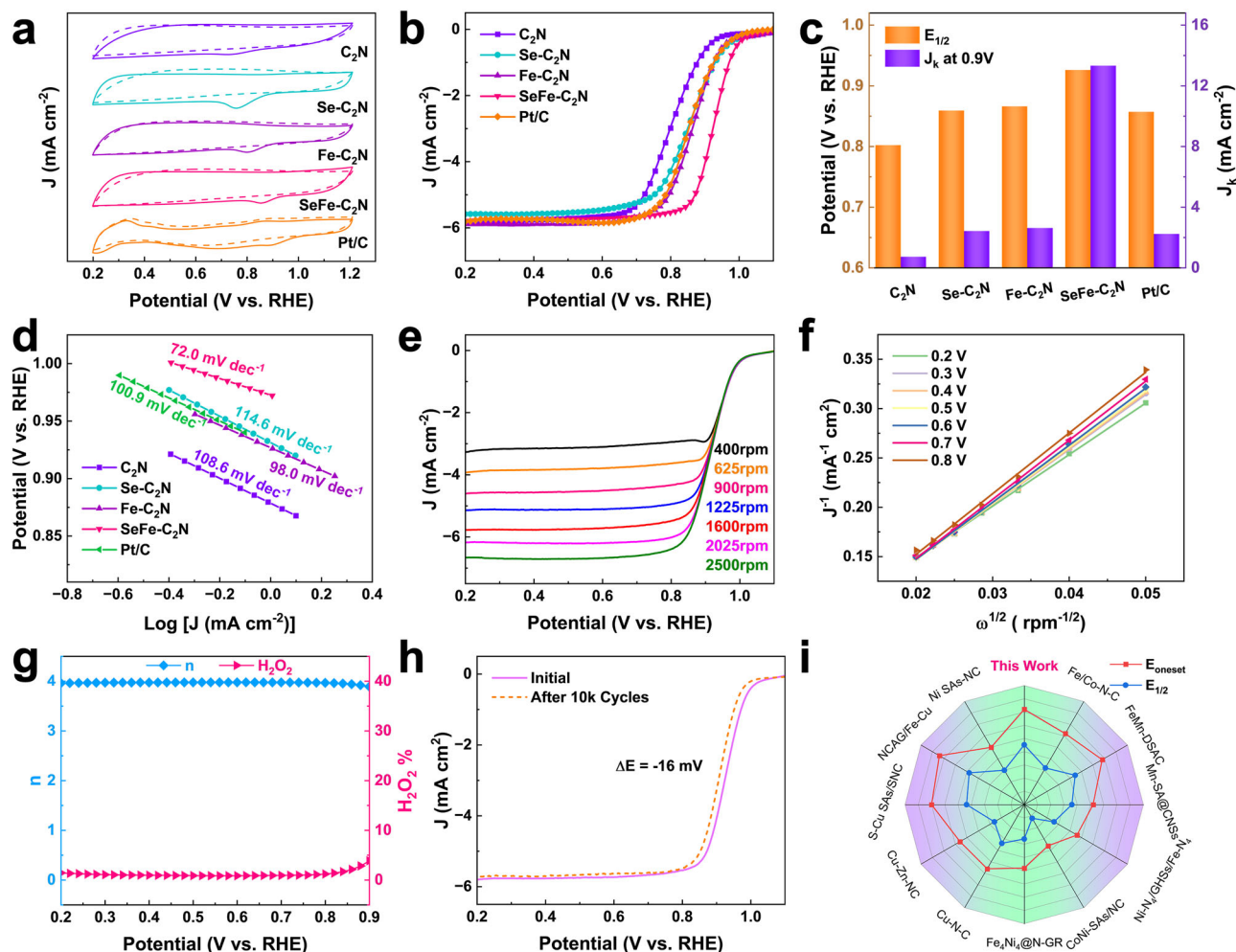


Fig. 3 | ORR electrochemical activity of SeFe-C₂N in 0.1 M KOH. a CV curves of in N₂ (dashed line) and O₂ (solid line). **b** ORR polarisation curves; series solution resistance (*R_s*) are 1.5, 2.0, 4.7, 3.3, and 3.2 Ω for C₂N, Se-C₂N, Fe-C₂N, SeFe-C₂N, and Pt/C, respectively. **c** Half-wave potential (*E*_{1/2}) and kinetic current density (*J_k*) at 0.9 V. **d** Corresponding Tafel plots. **e, f** LSV curves of SeFe-C₂N at various rotation

speeds (400–2500 rpm) and calculated K–L plots of SeFe-C₂N. **g** Electron transfer number and H₂O₂ selectivity of SeFe-C₂N. **h** Durability test of SeFe-C₂N for 10000 cycles. **i** Comparison of the catalytic activity of SeFe-C₂N with that of previously reported catalysts. All the potentials have not been *iR*-corrected.

electrochemical transfer resistance (35.2 Ω), which indicates a favourable charge transfer process. The electrochemical surface area (ECSA) can be determined via an electric double-layer capacitor (*C_{dl}*). The calculated *C_{dl}* of SeFe-C₂N is 33.95 mF cm⁻² (Supplementary Figs. 40–41), which is greater than that of the other samples, indicating a higher surface-active site density. To quantify a catalyst's inherent activity, the turnover frequency (TOF) is adopted, which is characterised as the conversion number of substrate molecules over one catalytic active site per unit time (s⁻¹ or h⁻¹). As shown in Supplementary Fig. 42, the obtained SeFe-C₂N presents a higher TOF value of 28.5 s⁻¹ than do Se-C₂N (19.0 s⁻¹) and Fe-C₂N (7.3 s⁻¹) at 0.9 V in 0.1 M KOH, suggesting the superior intrinsic ORR activity of SeN₂-FeN₂ moieties. Benefiting from the electronic redistribution and dual-atom synergistic effect, SeFe-C₂N also exhibited good methanol resistance (Supplementary Fig. 43). Additionally, long-term stability is another important criterion for electrocatalysts. Chronoamperometric measurements were conducted, and the current of SeFe-C₂N maintained 84% of the original value after 700 min of operation (Supplementary Fig. 44). After the accelerated durability test (ADT) in the potential range of 0.6–1.0 V for 10,000 CV cycles, the *E*_{1/2} of SeFe-C₂N was attenuated by only 16 mV, indicating a small decrease in catalytic activity (Fig. 3h). The morphology and composition of SeFe-C₂N after ADT were characterised via XPS, TEM, and HAADF-STEM

(Supplementary Figs. 45–47). Remarkably, no discernible aggregation or degradation occurs at the atomically distributed Se-Fe sites, indicating that synergistic dual-atom SeN₂-FeN₂ sites have long-term stability. Additional XAS measurements were implemented to evaluate the reversibility of the atomic coordination environment of the Se and Fe atoms in the SeFe-C₂N catalyst. As depicted in Supplementary Figs. 48–49, the XANES and EXAFS spectra of the Se K-edge and Fe K-edge remain almost the same before and after the reaction, demonstrating the recovery of the Se/Fe valence state and Se-N/Fe-N bond. The reversible change in the valence state and atomic coordination configuration for Fe and Se indicated the active contribution of Fe and Se atoms in the catalytic reaction for the ORR. As depicted in Fig. 3i and Supplementary Table 6, in comparison with recently reported catalysts, SeFe-C₂N has considerable potential for advancement in practical applications.

SeM-C₂N catalysts with other elements (M = Mn, Co, Ni, Cu, or Mo) were also fabricated to explore the universal regulatory effect of the Se modulator. The XRD patterns of the SeM-C₂N catalysts (Supplementary Fig. 50) show the absence of metal nanoparticles or metal oxide nanoparticles. Homologous distributions of C, N, Se, and other metal elements are observed from the EDS maps of the SeM-C₂N catalysts (Supplementary Figs. 51–55). High-resolution HAADF-STEM images of SeM-C₂N (Supplementary Figs. 56–60) reveal the successful

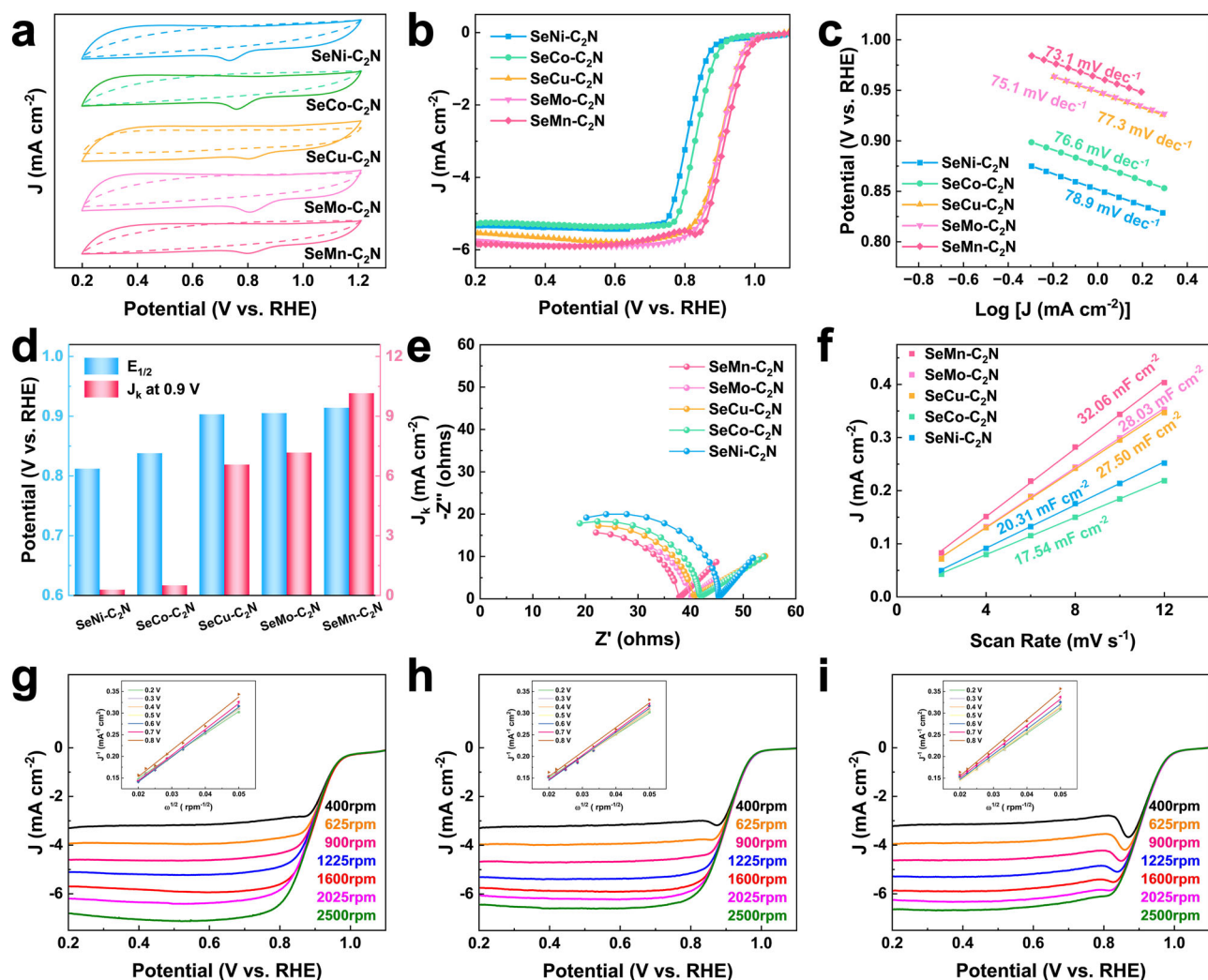


Fig. 4 | ORR electrochemical activity of SeM-C₂N (M = Mn, Co, Ni, Cu, Mo, etc.) in 0.1 M KOH. **a** CV curves of SeM-C₂N in N₂ (dotted line)- and O₂ (solid line)-saturated electrolytes. **b** ORR polarization curves; series solution resistance (*R_s*) are 3.8, 4.7, 6.8, 4.6, and 8.9 Ω for SeM-C₂N (M = Mn, Co, Ni, Cu, Mo), respectively.

c Tafel plots; **d** summary of *E*_{1/2} and *J_k*; **e** semicircular characteristics of the EIS curves; **f** *C*_{dil} values for all the samples. **g–i** LSV curves at different speeds (400–2500 rpm) and matching K–L plots at different potentials of SeCu-C₂N, SeMo-C₂N, and SeMn-C₂N, respectively. All the potentials have not been *iR*-corrected.

formation of dual atom sites (highlighted by yellow ellipses). They possess similar values of *I_D/I_G* (Supplementary Fig. 61) and a higher degree of graphitisation, which favour electron transfer, thus facilitating the ORR process. In addition, the high-resolution XPS spectra are shown in Supplementary Figs. 62–66. The predominant nitrogen species in SeMn-C₂N, SeCo-C₂N, SeNi-C₂N, SeCu-C₂N and SeMo-C₂N are still pyrrolic and pyrazine-like (44.59%, 41.62%, 44.99%, 43.49%, and 44.55%, respectively), which is analogous to SeFe-C₂N (45.72%, Supplementary Fig. 19c). In addition, the newly observed Se–M peaks in the Se 3*d* XPS spectra further confirm the electronic interaction between Se and other metal atoms. The measured XANES data from the SeM-C₂N (M represents Mn, Co, Ni, Cu, Mo) catalysts for the metal and Se are shown in Supplementary Figs. 67–71. The adsorption edge positions of the Mn/Co/Ni/Cu/Mo K-edge of the SeM-C₂N samples are located between those of the Mn foil and MnO₂ samples, Co foil and Co₃O₄ samples, Ni foil and NiO samples, Cu foil and CuO samples, and Mo foil and MoO₂ samples. These findings suggest that the average oxidation states of the metals Mn, Co, Ni, Cu, and Mo are 2.6, 2.7, 1.5, 1.7, and 1.4, respectively. The Se K-edges of the SeM-C₂N samples are located between those of the Se foil and SeO₂ samples, with average Se oxidation states of 0.7, 0.8, 0.6, 0.6 and 0.7 for SeMn-C₂N, SeCo-C₂N, SeNi-C₂N, SeCu-C₂N and SeMo-C₂N, respectively. The quantitative

EXAFS fitting results (Supplementary Figs. 72–77 and Supplementary Tables 7–8) at the Se and Mn/Fe/Co/Ni/Mo K-edges enable the extraction of specific structural parameters, which demonstrate the construction of asymmetric dual-atom SeN₂–MN₂ sites and reveal the synergistic effect between Se and other metal atoms.

Owing to the electronic regulation and synergistic effect of the Se modulator, the SeM-C₂N samples exhibit desirable ORR performance (Fig. 4a, b). With similar Tafel slopes (Fig. 4c), SeMn-C₂N, SeMo-C₂N, and SeCu-C₂N show ORR catalytic activities with *E*_{1/2} values of 0.914, 0.905, and 0.903 V, respectively, and enhanced *J_k* values (Fig. 4d), demonstrating the satisfactory electrocatalytic activity of asymmetrical SeN₂–MN₂ sites. In addition, SeM-C₂N possesses quick electron transfer ability (Fig. 4e) due to the charge redistribution of SeN₂–MN₂ and more exposure of activity sites (Supplementary Fig. 78 and Fig. 4f) caused by multiple pyrolyses. As illustrated in Fig. 4g–i, the electron transfer numbers (*n*) calculated from the K–L equation are 3.97, 3.96, and 3.94 for SeMn-C₂N, SeMo-C₂N, and SeCu-C₂N, respectively, which indicates the effectual four-electron-transfer route on the SeN₂–MN₂ catalysts.

To corroborate the practical application prospects of SeFe-C₂N, a homemade aqueous Zn–air battery (ZAB) was assembled with a SeFe-C₂N-modified gas diffusion layer as the cathode (Supplementary

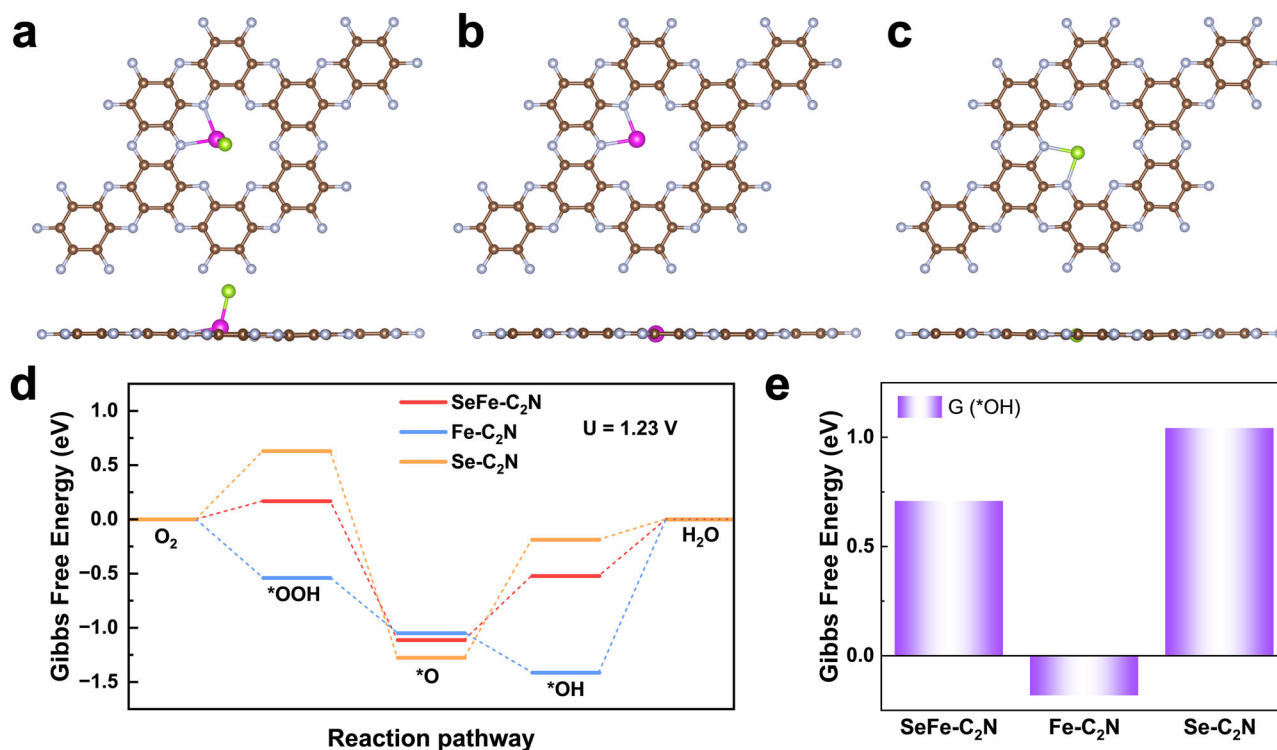


Fig. 5 | Theoretical calculation of the ORR. **a–c** Atomic configurations of SeFe-C₂N, Fe-C₂N and Se-C₂N, respectively. Brown, grey, purple and green atoms represent carbon, nitrogen, iron and selenium, respectively. **d** Gibbs free energy

diagram of the ORR on SeFe-C₂N, Fe-C₂N, and Se-C₂N. **e** Gibbs free energies of *OH adsorbed on SeFe-C₂N, Fe-C₂N, and Se-C₂N.

Fig. 79). As shown in Supplementary Fig. 80a, the SeFe-C₂N-based ZAB delivered a high opening voltage (1.50 V), considerably exceeding the open-circuit voltage of the Pt/C-based battery (1.37 V). Notably, the optimum SeFe-C₂N achieved a maximum power density of 287.2 mW cm⁻², which was higher than that of a commercial Pt/C-modified air electrode (194.2 mW cm⁻², Supplementary Fig. 80b). The specific capacity of the SeFe-C₂N-based ZAB at 5 mA cm⁻² is 764.8 mAh g⁻¹ (Supplementary Fig. 80c), which is superior to that of Pt/C (725.9 mAh g⁻¹). Moreover, the SeFe-C₂N-based battery could serve robustly for up to 50 h with minor discharge voltage attenuation (Supplementary Fig. 80d), which indicates the outstanding durability of the SeFe-C₂N-based Zn-air battery. To further validate the rechargeable stability of SeFe-C₂N, a long-term galvanostatic charge-discharge examination with an interval of 10 min each cycle was performed. The SeFe-C₂N + IrO₂-based rechargeable ZAB demonstrated a slight change in charge/discharge voltage in excess of 380 h at 10 mA cm⁻² (Supplementary Fig. 80e). In addition, a comparison of the performance of the as-assembled ZABs for recently reported catalysts indicates that SeFe-C₂N has remarkable activity and stability in practical applications (Supplementary Table 9).

Theoretical study of SeFe-C₂N on the ORR

To gain a deeper understanding of the high catalytic performance of SeFe-C₂N catalysts in the ORR process, the electrocatalytic reactivities of the SeFe-C₂N, Fe-C₂N, and Se-C₂N catalysts for the ORR were studied through density functional theory (DFT) calculations (Supplementary Data 1). Figure 5a–c illustrate the most stable configurations of the C₂N surface doped with Fe and nonmetallic Se atoms, single-atom Fe, and single-atom Se. Notably, unlike common dual-atom doping in C₂N, where doping atoms are typically found in the same plane, on the SeFe-C₂N surface, the Se atom and Fe-C₂N are not coplanar. We subsequently inspected the change in the Gibbs free energy along the ORR pathway at the equilibrium potential

(1.23 V) and different potential determination steps (PDSs) (Fig. 5d). The PDS of the Fe site on Fe-C₂N is the desorption of *OH, with $\Delta G = 1.41$ eV, which is consistent with previous research⁶¹. In comparison with Fe-C₂N, the nonmetallic doped Se-C₂N surface, which is also single-atom doped, has weak interactions with *OOH and *OH but strong interactions with *O. Consequently, the conversion of PDS on Se-C₂N involves the conversion of *O to *OH, and $\Delta G = 1.09$ eV. Unlike single-atom doping of Fe and Se, the codoping of Fe and Se can effectively regulate the adsorption strength of O-containing intermediates, making it more moderate on the SeFe-C₂N surface. After multiple attempts on the SeFe-C₂N surface, Se atoms were identified as the most stable adsorption sites during the ORR process (Supplementary Fig. 81).

First, the oxygen molecules adsorb and activate the Se site to form *OOH. During the second elementary reaction, the absorbed *OOH releases one OH⁻ after one electron is obtained, while the Se and Fe atoms coadsorb *O. This coadsorption formation reduces the thermodynamic energy barrier of *O to *OH after one H₂O and electron are obtained. Finally, *OH desorbs from the Se site while the last electron is obtained. The doping of Se not only altered the PDS of the original Fe-C₂N structure but also reduced the ΔG of the PDS from 1.41 eV to 0.59 eV, indicating satisfactory ORR catalytic functionality. The free energy diagram of the ORR clearly shows that the adsorption strength of the *OH intermediate plays a crucial role in the electrochemical activity of the ORR. Figure 5e clearly demonstrates that the over-binding of *OH on Fe-C₂N impedes its further conversion into H₂O, an important factor in decreasing the ORR efficiency. The weak adsorption of *OH on Se-C₂N is also unfavourable for the complete ORR. However, appropriate binding on the SeFe-C₂N surface ensures efficient ORR activity. In summary, the codoping of Se and Fe atoms appropriately increases the reactivity of Fe and Se single-atom doping, leading to more moderate adsorption on the substrate and more favourable thermodynamic conversion of O₂ to H₂O.

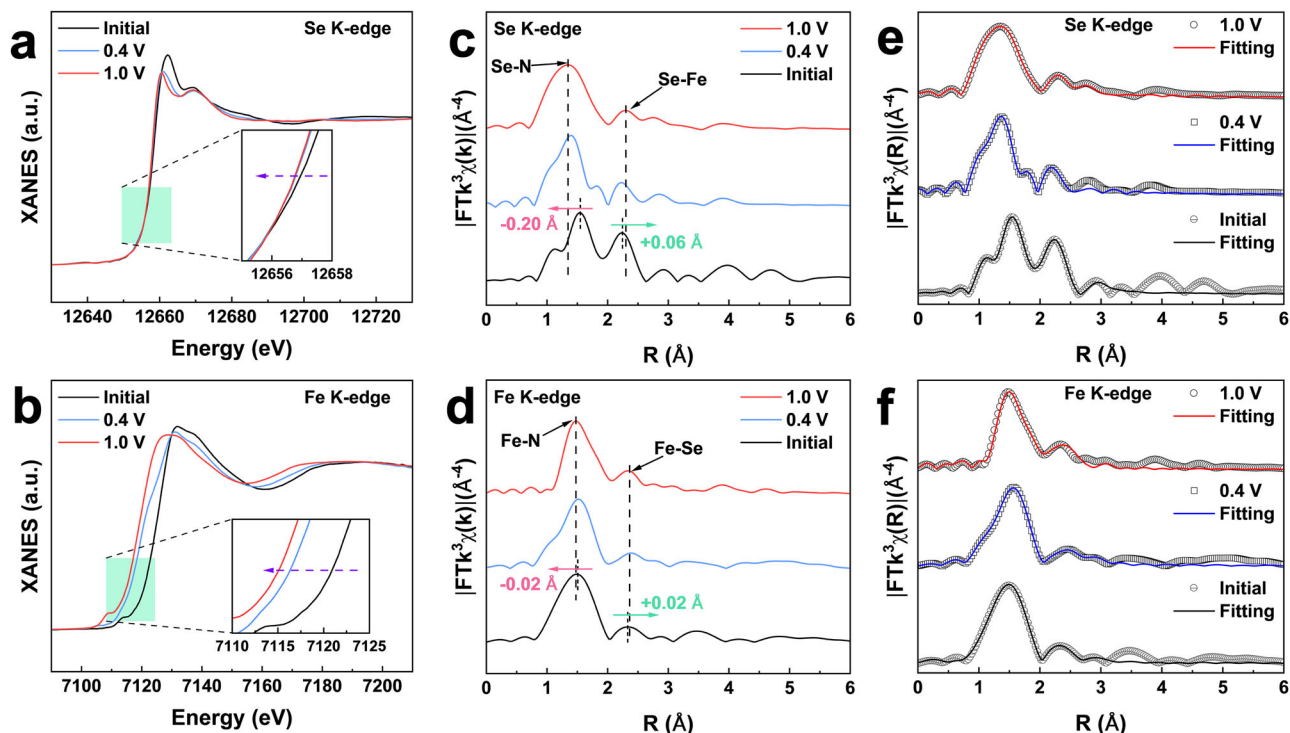


Fig. 6 | Operando XAS reveals the synergistic mechanism of SeFe-C₂N.

a, b Operando XANES spectra of SeFe-C₂N at the Se K-edge and Fe K-edge under several voltages. **c, d** FTs of k^3 -weighted operando EXAFS spectra of SeFe-C₂N at

the Se and Fe k-edges, respectively. **e, f** FT fitting curves in R space at the Se K-edge and Fe K-edge of SeFe-C₂N, respectively.

Operando XAS analysis

To explore the structural and electronic evolution of SeFe-C₂N in detail, operando XAS was performed under realistic device operation conditions (Supplementary Fig. 82)^{62,63}. Operando XANES spectra of the SeFe-C₂N catalysts at the Se K-edge and Fe K-edge were collected under several applied voltages, as presented in Fig. 6a, b, respectively. Compared with the pristine state, the E_0 position tends to negatively shift (-0.5 eV, Supplementary Fig. 83) with increasing cathodic voltage, indicating a reduced oxidation state of Se in working SeFe-C₂N. This phenomenon probably originates from electron transfer between Se and the adsorbed O-containing intermediate^{64,65}. Similarly, an obvious negative energy shift of 6.7 eV for E_0 is observed (Supplementary Fig. 84), which indicates that the valence state of Fe decreases after the adsorption of *O species.

The evolution of the atomic coordination configuration of the SeN₂-FeN₂ active site could be further identified through operando EXAFS. As shown in Fig. 6c, the intensities of the Se-Fe peaks considerably decrease as the applied voltage increases. In addition, an obvious low- R shift of the dominant Se-N peak from 1.55 Å to 1.35 Å and a slight high- R shift of the secondary Se-Fe peak from 2.24 Å to 2.30 Å can be observed. For the Fe sites, the Fe-Se bond length slightly expands, together with a slight low- R shift in the dominant Fe-N peak from 1.50 Å to 1.48 Å (Fig. 6d). Operando XANES and EXAFS results demonstrate that SeN₂-FeN₂ sites undergo structural evolution, which might be caused by the adsorption of oxygen intermediates during ZAB operation. Considering the adsorption of oxygen-containing species on SeN₂-FeN₂ sites revealed by DFT calculations and the differences in operando XANES spectra, Se-O and Fe-O scattering paths were added to fit the operando EXAFS quantitatively. As expected, the fitting curves of O atoms adsorbed on SeN₂-FeN₂ match well with the operando experimental data (Fig. 6e). Under an applied voltage of 1.0 V, Se is coordinated with approximately one N atom (Se-N, bond length of 1.80 Å), one Fe atom (Se-Fe, bond length of 2.58 Å), and one oxygen atom (Se-O, bond length

of 1.78 Å) (Supplementary Figs. 85 and Supplementary Table 10). Simultaneously, the first coordination sphere of Fe is also fitted as two Fe-N bonds ($R = 1.95$ Å), one Fe-Se bond ($R = 2.57$ Å), and one Fe-O bond ($R = 1.84$ Å) (Supplementary Fig. 86 and Supplementary Table 11). With increasing applied voltage and the successive processing of ORR catalysts, the coordination number of O around the Se and Fe sites increases, whereas the SeN₂-FeN₂ configuration undergoes a fine-tuning procedure with a small contraction strain of the Se-N bond. Overall, operando XAS further investigated the synergistic catalytic effect of SeN₂-FeN₂, which plays an important role in increasing the efficiency of the ORR process.

Discussion

In summary, asymmetric heteronuclear SeN₂-MN₂ dual-atom active sites anchored in C₂N (SeM-C₂N) have been successfully fabricated. Owing to the polarised charge distribution between the asymmetric Se and Fe moieties, the resulting SeFe-C₂N catalyst displays outstanding ORR performance, with an $E_{1/2}$ of 0.926 V in alkaline media. The orbital hybridization of the asymmetrical SeN₂-MN₂ dual atoms fine-tunes the energy of the intermediates adsorbed/desorbed at the active sites. SeFe-C₂N-based ZABs exhibit a comparable maximum power density of 287.2 mW cm⁻². Operando XAS analysis indicated that the Se-Fe dual atoms serve as cocatalytic sites. In addition, DFT calculations further revealed that the cocatalytic effect between SeN₂-FeN₂ dual-atom sites changes the potential determination steps and accelerates *OH formation. The rational design of innovative asymmetrical dual-atom site catalysts could inspire the manufacture and development of oxygen catalysts.

Methods

Chemicals

All chemicals utilized in this experiment were commercially available and used directly without additional purification. Cyclohexanhexone octahydrate (C₆O₆·8H₂O, 99%, Aladdin), Urea (CH₄N₂O, 99%,

Kemiou), Magnesium chloride (MgCl₂, 99%, Aladdin), Sulphuric acid (H₂SO₄, 98%, XiLong Scientific), Iron(III) acetylacetonate (C₁₅H₂₁FeO₆, 98%, Aladdin), Manganese(II) acetylacetonate (C₁₀H₁₄MnO₄, 97%, Macklin), Cobalt(II) acetylacetonate (C₁₀H₁₄O₄Co, 97%, Macklin), Nickel(II) acetylacetonate (NiC₁₀H₁₄O₄, 95%, Macklin), Copper(II) acetylacetonate (C₁₀H₁₄CuO₄, 97%, Macklin), Bis(acetylacetonato)dioxomolybdenum(VI) (C₁₀H₁₄MoO₆, 97%, Macklin), Vulcan XC-72R carbon black (CAS No.: 1333-86-4, SCI Materials Hub) commercial Pt/C (20 wt%, Alfa Aesar), Ethanol (CH₃CH₂OH, 99.7%, Tianjin Fuyu Fine Chemical Co., Ltd), Nafion 117 solution (~5% in a mixture of lower aliphatic alcohols and water, Aladdin). The purity levels of oxygen and nitrogen gases are 99.999%.

Preparation of C₂N

The initial step involved the preparation of a thoroughly ground mixture of cyclohexanehexone and urea with a molar ratio of 1:4.5. This mixture was then gently heated at 90 °C for 0.5 h. Following this, the formed cross-linked product and anhydrous MgCl₂ were ground together with a mass ratio of 1:3.75. Subsequently, the resulting powder underwent calcination at temperatures of 500, 800, 900, and 1000 °C for 2 h, utilising a heating rate of 3 °C min⁻¹ under nitrogen protection. Upon reaching room temperature, the carbon samples were subjected to a series of washes using sulphuric acid (H₂SO₄, 0.5 M), deionized water, and ethanol in succession. Following overnight drying in a vacuum oven at 60 °C, the C₂N-500, C₂N-800, C₂N-900, and C₂N-1000 samples were obtained.

Preparation of Fe–C₂N

The 90 mg of as-obtained C₂N was mixed with 6 mg Iron(III) acetylacetonate through the grinding method. Subsequently, the powder was transferred in a tube furnace under a flowing nitrogen atmosphere to a temperature of 900 °C at 3 °C min⁻¹. The obtained material was then annealed for 2 h. Following natural cooling to room temperature, Fe–C₂N was synthesised and employed directly without any additional treatment.

Preparation of Se–C₂N

The selenium dioxide (SeO₂) and C₂N (a mass ratio of 1:1) were mixed and fully ground into a homogeneous powder. Subsequently, the powder was heated in a tube furnace under a flowing nitrogen atmosphere. The temperature was initially raised to 300 °C for 30 min, subsequently increased to 1000 °C at 5 °C min⁻¹ and maintained for 1 h. After natural cooling to room temperature, Se–C₂N was synthesised and utilised directly without any additional treatment.

Preparation of SeM–C₂N

A total of 90 mg of the as-obtained Se–C₂N was mixed with 6 mg of iron(III) acetylacetonate through the grinding method. Subsequently, the powder was heated in a tube furnace under a flowing nitrogen atmosphere to a temperature of 900 °C at 3 °C min⁻¹. The material was then subjected to annealing for a duration of 2 h. Following natural cooling to room temperature, SeFe–C₂N was obtained and directly used without further treatment. For SeMn–C₂N, SeCo–C₂N, SeNi–C₂N, SeCu–C₂N, and SeMo–C₂N, these samples were prepared as control groups via a similar approach as SeFe–C₂N, except that diverse metal salts were added in the same molar amount.

Preparation of Se–C₂N-2nd and Fe–C₂N-2nd

The Se–C₂N and Fe–C₂N catalysts were subjected to additional pyrolysis treatment. Specifically, they were annealed at 900 °C and 1000 °C respectively, for a duration of 2 h under a flowing nitrogen atmosphere with 3 °C min⁻¹. The resulting catalysts are designated as Se–C₂N-2nd and Fe–C₂N-2nd, respectively.

Preparation of Fe/C materials

Vulcan XC-72R carbon black (CAS No.: 1333-86-4) with average particle size of ~50 nm was selected as the substrate. In a typical synthetic process, 90 mg Vulcan XC-72R carbon black and 6, 18, and 30 mg Iron(III) acetylacetonate were sonicated in ethanol, respectively. After completely evaporating ethanol under heating and stirring, the obtained mixed powders were heated in a tube furnace under a flowing nitrogen atmosphere to a temperature of 900 °C at 3 °C min⁻¹. The material was then subjected to annealing for a duration of 2 h. Following natural cooling to room temperature, Fe/C-1, Fe/C-3, and Fe/C-5 were obtained.

Characterisations

The Bruker D8 Advance and a Rigaku Ultima IV were employed to perform the XRD experiments. The Raman spectra were acquired using a LabRAM HR Evo spectrometer equipped with a 532 nm He-Ne laser. XPS measurements were performed using an Escalab 250Xi electron spectrometer equipped with Al K α radiation. The N₂ adsorption-desorption isotherms conducted at 77 K using a BELSORP MAX G instrument was performed to determine the specific surface areas and pore size distributions of the samples. The chemical structures of the samples were characterised using FTIR spectroscopy with a Bruker Tensor II spectrometer. Thermogravimetric mass spectrometry (TGA–MS) measurements were performed on Pyris Diamond /OmniStarTM. The TEM analysis was performed on the FEI Talos F200S emission scanning electron microscope. HAADF-STEM was performed using a JEOL JEM-ARM200CF microscope, which operated at 200 kV and was equipped with a Schottky cold-field emission gun. ICP–OES analysis was performed using a Shimadzu ICPE-9820 instrument. The Se K-edge and Fe K-edge X-ray absorption data were collected at BL1W1B and 4B7B stations in the Beijing Synchrotron Radiation Facility (BSRF).

Electrochemical measurements for the ORR

All electrochemical tests were carried out at room temperature using a CHI 760E (CH Instrument Co., Ltd., Shanghai, China) fitted with a speed controller (Pine Co., Ltd., USA). 0.1 M KOH electrolyte (pH = 12.9 ± 0.13) was prepared by dissolving 2.95 g of 95% pure KOH in 500 mL of deionized water with continuous agitation to ensure complete dissolution. The experiment was conducted using a three-electrode system. The working electrode consisted of a glassy carbon rotating disk electrode (GC-RDE) with a disk diameter of 5 mm (geometric surface area: 0.19625 cm²), which was coated with the catalyst. The reference electrode was a saturated calomel electrode (SCE), and the counter electrode was a platinum electrode. The electrocatalyst ink was prepared by dispersing 2 mg of catalyst into a solution consisting of 180 μ L of ethanol, 60 μ L of deionized water, and 10 μ L of Nafion (5 wt%). Subsequently, 10 μ L of homogeneous ink was dropped on the freshly polished GC-RDE glass carbon electrode (0.4 mg cm²) and allowed to dry naturally. CV tests with N₂/O₂-saturated electrolytes were performed at a scan rate of 50 mV s⁻¹. LSV measurements were performed at a scan rate of 5 mV s⁻¹ in an O₂-saturated solution with variable rotation speeds ranging from 400 to 2025 rpm. All the potentials have not been *iR*-corrected. According to the Nernst equation, all of the potentials were calibrated to the reversible hydrogen electrode (RHE):

$$E_{\text{RHE}} = E_{\text{SCE}} + 0.2415 + 0.0592 \times \text{pH} \quad (1)$$

Further information of SCE calibration referred to RHE was shown in Supplementary Note 1. The solution resistance (*R*_s) and charge transfer resistance were assessed using electrochemical impedance spectroscopy (EIS) across a frequency range of 10⁶ to 0.01 Hz, with an applied amplitude of 5 mV at the open circuit potential (OCP). Durability tests were performed by cycling between 0.6 and 1.0 V versus

RHE for 10,000 cycles at room temperature. The long-term stability test was conducted on the basis of the chronoamperometric response (CA) at 0.8 V vs. RHE with rotation speeds 1600 rpm. The C_{dl} was obtained from the CV curves in the nonfaradaic region at various scan rates (2 to 12 mV s⁻¹). During RDE measurements, the Koutecky–Levich (K–L) equation was employed to determine the kinetic current density (J_k) and the number of electrons transferred (n)

$$\frac{1}{J} = \frac{1}{J_L} + \frac{1}{J_k} = \frac{1}{B\omega^{1/2}} + \frac{1}{J_k} \quad (2)$$

$$B = 0.62nFC_0D_0^{2/3}\nu^{-1/6} \quad (3)$$

Where J_k , J_L and J represent the kinetic current density, diffusion-limiting current density and measured current, respectively; ω represents the angular velocity for the disk ($2\pi N$, where N is the rotation speed); C_0 is the bulk concentration of O₂ (1.2×10^{-6} mol cm⁻³); F is the Faraday constant (96485 C mol⁻¹); ν is the kinetic viscosity (0.01 cm²s⁻¹); and n is the electron transfer number of the ORR process; D_0 is the diffusion coefficient of O₂ (1.9×10^{-5} cm² s⁻¹).

For the RRDE measurements, the yield of hydrogen peroxide (H₂O₂) and the electron transfer number (n) were determined via the following equations:

$$n = \frac{4 \times I_d}{I_d + I_r/N} \quad (4)$$

$$H_2O_2(\%) = 200 \times \frac{I_r/N}{I_d + I_r/N} \quad (5)$$

where I_r and I_d are the ring current and disk current, respectively. N is the ring collection efficiency ($N = 0.37$). RRDE tests were performed to investigate the 4e⁻ selectivity of the samples with a ring electrode potential of 1.23 V vs. RHE.

The calculation formula for the TOF is as follows:

$$\text{TOF}[\text{site}^{-1}\text{s}^{-1}] = \frac{J_k \times N_e}{C_{\text{cat}} \times \omega_{\text{metal}} \times M_{\text{metal}} \times N_A} \quad (6)$$

where N_e is the electron number per Coulomb (6.24×10^{18}), J_k is the kinetic current density, C_{cat} is the catalyst loading, ω_{metal} is the metal content of the samples, M_{metal} is the molar mass of the metal, and N_A is the Avogadro number (6.022×10^{23}).

Above all key derived or measured values of ORR measurements were only performed once.

Zn–air battery measurements

In this assembly, the anode of the Zn–air battery is made of polished zinc foil with a thickness of 0.5 mm. The mixed aqueous solution composed of 6 M KOH and 0.2 M Zn(CH₃COO)₂ was act as the electrolyte. The SeFe–C₂N catalyst ink was uniformly applied to conductive carbon paper to fabricate the air cathode with a loading of 1 mg cm⁻². 20% Pt/C was used as the control electrocatalyst for comparison. The discharge polarisation curve was collected at a scan rate of 5 mV s⁻¹ using the CHI 760E. The cycling stability tests for charging and discharging were conducted at 10 mA cm⁻², with each cycle lasting 10 min, utilising a LANHE CT3002A multi-channel battery testing instrument.

DFT calculation

Our computational simulations were conducted using the Vienna Ab-initio Simulation Package (VASP), employing projector augmented wave (PAW) pseudopotentials to characterise the interactions between atomic cores and valence electrons within the framework of density functional theory (DFT + U)^{66–68}. The exchange–correlation energy was

computed using the generalised gradient approximation (GGA) of the Perdew–Burke–Ernzerhof (PBE) functional⁶⁹. To sample the Brillouin zone, the k point was set to $2 \times 3 \times 1$ gamma point grid, with a cut-off energy of the plane wave orbit set to 520 eV. The convergence criterion of the force calculation and energy calculation were 10^{-5} eV Å⁻¹ and 3×10^{-2} eV, respectively. The SeFe–C₂N model contains 48 C atoms, 24 N atoms, 1 Fe atom, and 1 Se atom. Vacuum space was set larger than 15 Å along the vertical direction to avoid the interaction between interlayers. In the ORR process, molecular oxygen was simplified into four basic steps to form water and generate electric energy, the Gibbs free energy (ΔG) of each reaction step can be expressed as follows⁷⁰:

$$\Delta G = \Delta E - \Delta ZPE - T\Delta S + \Delta G_U \quad (7)$$

where ΔE represents the energy difference between the intermediates before and after adsorption on the catalyst surface. ΔZPE is the zero-point energy difference, $T\Delta S$ the entropy change. $\Delta G_U = -eU$ was used to consider the electric potential.

XAFS measurements and processing

Utilise the ATHENA module within the IFEFFIT package to process EXAFS data in accordance with established protocols⁷¹. Firstly, the data were imported using the following equation:

$$\text{Transmission mode : } u = -\ln\left(\frac{I}{I_0}\right) \quad (8)$$

$$\text{Fluorescence mode : } u_F = \frac{I_F}{I_0} \quad (9)$$

u and u_F are the experimental data, I_0 is the Incident light intensity, I and I_F are the detected light intensity.

Subsequently, the experimental data $u_T(E)$ was collected. After performing the background subtraction and normalisation, the normalised curve $u_T(E)$ was derived. The data was then subjected to E_0 and $E-k$ transformations to convert it into k -space, yielding $u(k)$. Following this, the oscillation function $\chi(k)$ was extracted. Through Fourier transformation with a Hanning window $dk = 1.0 \text{ \AA}^{-1}$, the radial distribution function was obtained. The precise coordination parameters of the central atom were determined through least-squares curve fitting utilising the ARTEMIS module within the IFEFFIT software suite:

$$\chi(k) = \sum_j \frac{N_j S_0^2 F_j(k)}{k R_j^2} \exp[-2k^2 \sigma_j^2] \exp\left[\frac{-2R_j}{\lambda(k)}\right] \sin[2kR_j + \phi_j(k)] \quad (10)$$

The coordination number N , Debye–Waller factor σ^2 , amplitude reduction factor S_0^2 are correlated with peak strength. In contrast, the interatomic spacing R and ΔE_0 are associated with peak position.

$$k = \frac{1}{\hbar} \sqrt{2m_e \Delta E_0} \quad (11)$$

The scattering amplitude $F(k)$, phase shift $\phi(k)$, and mean free path are typically determined through Feff calculations. The amplitude reduction parameter S_0^2 was fixed by the foil sample. The error bars determined by EXAFS fitting were as follows: $N \pm 20\%$, $R \pm 1\%$, $\sigma^2 \pm 20\%$, and $\Delta E_0 \pm 20\%$. Additional details regarding the processing of XAFS data are provided in Supplementary Note 2.

Data availability

All data supporting the findings of this study are available within the paper and its supplementary information files or from the corresponding authors upon request. Source data are provided with this paper.

References

1. Wang, J. et al. Micromechanism in all-solid-state alloy-metal batteries: regulating homogeneous lithium precipitation and flexible solid electrolyte interphase evolution. *J. Am. Chem. Soc.* **143**, 839–848 (2021).
2. Debe, M. Electrocatalyst approaches and challenges for automotive fuel cells. *Nature* **486**, 43–51 (2012).
3. Tang, C. et al. Defect engineering toward atomic Co–N_x–C in hierarchical graphene for rechargeable flexible solid Zn–air batteries. *Adv. Mater.* **29**, 1703185 (2017).
4. Gao, R. et al. Pt/Fe₂O₃ with Pt–Fe pair sites as a catalyst for oxygen reduction with ultralow Pt loading. *Nat. Energy* **6**, 614–623 (2021).
5. Shang, H. et al. Atomic design of carbon-based dual-metal site catalysts for energy applications. *Nano Res* **16**, 6477–6506 (2023).
6. Song, Z. et al. Progress and perspective of single-atom catalysts for membrane electrode assembly of fuel cells. *Carbon Energy* **5**, e342 (2023).
7. Xiao, F. et al. Recent advances in electrocatalysts for proton exchange membrane fuel cells and alkaline membrane fuel cells. *Adv. Mater.* **33**, 2006292 (2021).
8. Lim, B. et al. Pd–Pt bimetallic nanodendrites with high activity for oxygen reduction. *Science* **324**, 1302–1305 (2009).
9. Ahsan, M. A. et al. Tuning of trifunctional NiCu bimetallic nanoparticles confined in a porous carbon network with surface composition and local structural distortions for the electrocatalytic oxygen reduction, oxygen and hydrogen evolution reactions. *J. Am. Chem. Soc.* **142**, 14688–14701 (2020).
10. Zitolo, A. et al. Identification of catalytic sites for oxygen reduction in iron- and nitrogen-doped graphene materials. *Nat. Mater.* **14**, 937–942 (2015).
11. Qiao, B. et al. Single-atom catalysis of CO oxidation using Pt₁/FeO_x. *Nat. Chem.* **3**, 634–641 (2011).
12. Ding, S. et al. Transforming energy with single-atom catalysts. *Joule* **3**, 2897–2929 (2019).
13. Chen, C. et al. Dual-metal single-atomic catalyst: the challenge in synthesis, characterization, and mechanistic investigation for electrocatalysis. *SmartMat* **3**, 533–564 (2022).
14. Shang, H. et al. Engineering unsymmetrically coordinated Cu–S₁N₃ single atom sites with enhanced oxygen reduction activity. *Nat. Commun.* **11**, 3049 (2020).
15. Qin, S. et al. Fe–Co–Ni ternary single-atom electrocatalyst and stable quasi-solid-electrolyte enabling high-efficiency zinc-air batteries. *Nano Res. Energy* **3**, e9120122 (2024).
16. Wang, X. et al. Electronic structure regulation of the Fe-based single-atom catalysts for oxygen electrocatalysis. *Nano Energy* **121**, 109268 (2024).
17. Li, J. et al. Identification of durable and non-durable FeN_x sites in Fe–N–C materials for proton exchange membrane fuel cells. *Nat. Catal.* **4**, 10–19 (2021).
18. Liu, S. et al. Atomically dispersed iron sites with a nitrogen–carbon coating as highly active and durable oxygen reduction catalysts for fuel cells. *Nat. Energy* **7**, 652–663 (2022).
19. Wan, X. et al. Iron atom-cluster interactions increase activity and improve durability in Fe–N–C fuel cells. *Nat. Commun.* **13**, 2963 (2022).
20. Zhong, X. et al. Engineering Pt and Fe dual-metal single atoms anchored on nitrogen-doped carbon with high activity and durability towards oxygen reduction reaction for zinc-air battery. *Appl. Catal. B* **286**, 119891 (2021).
21. Zhang, W. et al. Emerging dual-atomic-site catalysts for efficient energy catalysis. *Adv. Mater.* **33**, 2102576 (2021).
22. Yang, Y. et al. O-coordinated W–Mo dual-atom catalyst for pH-universal electrocatalytic hydrogen evolution. *Sci. Adv.* **6**, eaba6586 (2020).
23. Zhang, L. et al. High-density asymmetric iron dual-atom sites for efficient and stable electrochemical water oxidation. *Nat. Commun.* **15**, 9440 (2024).
24. Pei, J. et al. Integrating host design and tailored electronic effects of yolk-shell Zn–Mn diatomic sites for efficient CO₂ electroreduction. *Angew. Chem. Int. Ed.* **63**, e202316123 (2024).
25. Cheng, Y. et al. Design strategies towards transition metal single atom catalysts for the oxygen reduction reaction – A review. *Nano Res. Energy* **2**, e9120082 (2023).
26. Zhong, G. et al. Atomically dispersed Mn–Nx catalysts derived from Mn-hexamine coordination frameworks for oxygen reduction reaction. *Carbon Energy* **6**, e484 (2024).
27. Wang, J. et al. Non-precious-metal catalysts for alkaline water electrolysis: operando characterizations, theoretical calculations, and recent advances. *Chem. Soc. Rev.* **49**, 9154–9196 (2020).
28. Pu, T. et al. Dual atom catalysts for energy and environmental applications. *Angew. Chem. Int. Ed.* **62**, e202305964 (2023).
29. Liu, M. et al. Ferredoxin-inspired design of S-synergized Fe–Fe dual-metal center catalysts for enhanced electrocatalytic oxygen reduction reaction. *Adv. Mater.* **36**, 2309231 (2024).
30. Wu, X.-G. et al. FeCo–N encapsulated in nitrogen-doped carbon nanotubes as bifunctional electrocatalysts with a high stability for zinc air batteries. *Rare Met* **42**, 1526–1534 (2023).
31. Zhang, Y.-X. et al. General synthesis of a diatomic catalyst library via a macrocyclic precursor-mediated approach. *J. Am. Chem. Soc.* **145**, 4819–4827 (2023).
32. Zhou, X. et al. Theoretically revealed and experimentally demonstrated synergistic electronic interaction of CoFe dual-metal sites on N-doped carbon for boosting both oxygen reduction and evolution reactions. *Nano Lett.* **22**, 3392–3399 (2022).
33. Li, H. et al. Enhanced Fe 3d delocalization and moderate spin polarization in Fe–Ni atomic pairs for bifunctional ORR and OER electrocatalysis. *Appl. Catal. B* **285**, 119778 (2021).
34. Liu, Y. et al. Optimizing Fe-3d electron delocalization by asymmetric Fe–Cu diatomic configurations for efficient anion exchange membrane fuel cells. *Adv. Energy Mater.* **13**, 2302719 (2023).
35. Li, H. et al. A durable half-metallic diatomic catalyst for efficient oxygen reduction. *Energy Environ. Sci.* **15**, 1601–1610 (2022).
36. Yang, G. et al. Regulating Fe-spin state by atomically dispersed Mn–N in Fe–N–C catalysts with high oxygen reduction activity. *Nat. Commun.* **12**, 1734 (2021).
37. Zhu, P. et al. Regulating the FeN₄ moiety by constructing Fe–Mo dual-metal atom sites for efficient electrochemical oxygen reduction. *Nano Lett.* **22**, 9507–9515 (2022).
38. Iqbal, M. S. et al. Single-atom catalysts for electrochemical N₂ reduction to NH₃. *Rare Met* **42**, 1075–1097 (2023).
39. Zong, L. et al. Promoting oxygen reduction reaction on atomically dispersed Fe sites via establishing hydrogen bonding with the neighboring P atoms. *Adv. Energy Mater.* **13**, 2203611 (2023).
40. Bhunia, S. et al. Rational design of mononuclear iron porphyrins for facile and selective 4e[−]/4H⁺ O₂ reduction: activation of O–O bond by 2nd sphere hydrogen bonding. *J. Am. Chem. Soc.* **140**, 9444–9457 (2018).
41. Sun, Z. et al. Understanding synergistic catalysis on Cu–Se dual atom sites via operando X-ray absorption spectroscopy in oxygen reduction reaction. *Angew. Chem. Int. Ed.* **62**, e202217719 (2023).
42. Sun, K. et al. Nature-inspired design of molybdenum-selenium dual-single-atom electrocatalysts for CO₂ reduction. *Adv. Mater.* **34**, 2206478 (2022).

43. Niu, Z. et al. Long-range regulation of Se doping for oxygen reduction of atomically dispersed Sb catalysts for ultralow-temperature solid-state Zn-air batteries. *ACS Catal.* **13**, 7122–7131 (2023).
44. Chen, X. et al. Pre-adsorption of chlorine enhances the oxyphilic property and oxygen reduction activity of Fe/Se-NC electrocatalyst in seawater electrolyte. *Chem. Eng. J.* **482**, 148856 (2024).
45. Mahmood, J. et al. Nitrogenated holey two-dimensional structures. *Nat. Commun.* **6**, 6486 (2015).
46. Fechler, N. et al. Eutectic syntheses of graphitic carbon with high pyrazinic nitrogen content. *Adv. Mater.* **28**, 1287–1294 (2016).
47. Hu, X. et al. Versatile, aqueous soluble C₂N quantum dots with enriched active edges and oxygenated groups. *J. Am. Chem. Soc.* **142**, 4621–4630 (2020).
48. Zhong, W. et al. Electronic spin moment as a catalytic descriptor for Fe single-atom catalysts supported on C₂N. *J. Am. Chem. Soc.* **143**, 4405–4413 (2021).
49. Xu, W. et al. Coordinatively unsaturated single Co atoms immobilized on C₂N for efficient oxygen reduction reaction. *Nano Res* **16**, 2294–2301 (2023).
50. Zhang, L. et al. Hybrid double atom catalysts for hydrogen evolution reaction: a sweet marriage of metal and nonmetal. *Adv. Energy Mater.* **14**, 2302754 (2024).
51. Wang, X. et al. p-d orbital hybridization induced by asymmetrical FeSn dual atom sites promotes the oxygen reduction reaction. *J. Am. Chem. Soc.* **146**, 21357–21366 (2024).
52. Yao, D. et al. Inter-metal interaction with a threshold effect in NiCu dual-atom catalysts for CO₂ electroreduction. *Adv. Mater.* **35**, 2209386 (2023).
53. Yi, J.-D. et al. Atomically dispersed iron-nitrogen active sites within porphyrinic triazine-based frameworks for oxygen reduction reaction in both alkaline and acidic media. *ACS Energy Lett.* **3**, 883–889 (2018).
54. Hu, H. et al. Atomically dispersed selenium sites on nitrogen-doped carbon for efficient electrocatalytic oxygen reduction. *Angew. Chem. Int. Ed.* **61**, e202114441 (2022).
55. Wang, Y. et al. Synergistic Fe–Se atom pairs as bifunctional oxygen electrocatalysts boost low-temperature rechargeable Zn-air battery. *Angew. Chem. Int. Ed.* **62**, e202219191 (2023).
56. Yi, Y. et al. A new dynamic covalent bond of Se–N: towards controlled self-assembly and disassembly. *Chem. Eur. J.* **19**, 9506–9510 (2013).
57. Yang, H. et al. Atomically dispersed Ni(I) as the active site for electrochemical CO₂ reduction. *Nat. Energy* **3**, 140–147 (2018).
58. Han, A. et al. An adjacent atomic platinum site enables single-atom iron with high oxygen reduction reaction performance. *Angew. Chem. Int. Ed.* **60**, 19262–19271 (2021).
59. Ravel, Y. & Newville, M. ATHENA and ARTEMIS: interactive graphical data analysis using IFEFFIT. *Phys. Scr.* **2005**, 1007 (2005).
60. Tafel, J. et al. Über die polarisation bei kathodischer Wasserstoffentwicklung. *Phys. Chem.* **50U**, 641–712 (1905).
61. Shu, D. et al. Non-metal doped Fe–C₂N as an electrocatalyst for oxygen reduction reaction: a density functional calculation. *N. J. Chem.* **47**, 20151–20156 (2023).
62. Luo, Y. et al. Stabilized hydroxide-mediated nickel-based electrocatalysts for high-current-density hydrogen evolution in alkaline media. *Energy Environ. Sci.* **14**, 4610–4619 (2021).
63. Friebe, D. et al. Balance of nanostructure and bimetallic interactions in Pt model fuel cell catalysts: in situ XAS and DFT study. *J. Am. Chem. Soc.* **134**, 9664–9671 (2012).
64. Han, G. et al. Substrate strain tunes operando geometric distortion and oxygen reduction activity of CuN₂C₂ single-atom sites. *Nat. Commun.* **12**, 6335 (2021).
65. Tong, M. et al. Operando cooperated catalytic mechanism of atomically dispersed Cu–N₄ and Zn–N₄ for promoting oxygen reduction reaction. *Angew. Chem. Int. Ed.* **60**, 14005–14012 (2021).
66. Blöchl, P. E. Projector augmented-wave method. *Phys. Rev. B* **50**, 17953 (1994).
67. Bajdich, M. et al. Theoretical investigation of the activity of cobalt oxides for the electrochemical oxidation of water. *J. Am. Chem. Soc.* **135**, 13521–413530 (2013).
68. Kresse, G. & Furthmüller, J. Efficiency of ab-initio total energy calculations for metals and semiconductors using a plane-wave basis set. *Comput. Mater. Sci.* **6**, 15–50 (1996).
69. Perdew, J. P. et al. Generalized gradient approximation made simple. *Phys. Rev. Lett.* **77**, 3865–3868 (1996).
70. Nørskov, J. K. et al. Origin of the overpotential for oxygen reduction at a fuel-cell cathode. *J. Phys. Chem. B* **108**, 17886–17892 (2004).
71. Yang, T. et al. Atomically dispersed Ru in Pt₃Sn intermetallic alloy as an efficient methanol oxidation electrocatalyst. *Chem. Commun.* **57**, 2164–2167 (2021).

Acknowledgements

This work was supported by the National Natural Science Foundation of China (Grant Nos. 22201262 to H.S., U22A20143 to B.Z., 22375019 to W.C., and 22103047 to L.Z. (Liang Zhang)), the Beijing Institute of Technology Research Fund Programme for Young Scholars (2022CX01011 to W.C.) and the China Postdoctoral Science Foundation (No. 2021M701864 to X.L.). State Key Laboratory of Intelligent Green Vehicle and Mobility under Project No. ZZ2023-063 to L.Z. (Liang Zhang), Tsinghua University Student Research Training Programme, Dushi Programme and Initiative Scientific Research Programme. The authors thank the Centre for Advanced Analysis and Gene Sequencing of Zhengzhou University and BL1W1B and 4B7B in the Beijing Synchrotron Radiation Facility (BSRF), BL14W1 in the Shanghai Synchrotron Radiation Facility (SSRF) and Tsinghua Centre of High Performance Computing for help with characterisations and computations.

Author contributions

H.S. and W.C. conceived the study, designed the study, and wrote the paper. X.W. and N.Z. performed the sample synthesis, performed most of the reactions, collected and analysed the data, and wrote the paper. W.C. and Z.S. carried out the X-ray absorption fine structure characterisations and data analysis. X.W., L.Z. (Lili Zhang) and Y.L. conducted the electrochemical measurements. H.D., X.L. and L.Z. (Liang Zhang) performed the DFT calculations. B.Z. helped to check and revise the paper.

Competing interests

The authors declare that they have no competing interests.

Additional information

Supplementary information The online version contains supplementary material available at <https://doi.org/10.1038/s41467-025-55862-6>.

Correspondence and requests for materials should be addressed to Huishan Shang, Xuan Luo or Wenxing Chen.

Peer review information *Nature Communications* thanks Nicolas Alonso-Vante, and the other, anonymous, reviewer(s) for their contribution to the peer review of this work. A peer review file is available.

Reprints and permissions information is available at <http://www.nature.com/reprints>

Publisher's note Springer Nature remains neutral with regard to jurisdictional claims in published maps and institutional affiliations.

Open Access This article is licensed under a Creative Commons Attribution-NonCommercial-NoDerivatives 4.0 International License, which permits any non-commercial use, sharing, distribution and reproduction in any medium or format, as long as you give appropriate credit to the original author(s) and the source, provide a link to the Creative Commons licence, and indicate if you modified the licensed material. You do not have permission under this licence to share adapted material derived from this article or parts of it. The images or other third party material in this article are included in the article's Creative Commons licence, unless indicated otherwise in a credit line to the material. If material is not included in the article's Creative Commons licence and your intended use is not permitted by statutory regulation or exceeds the permitted use, you will need to obtain permission directly from the copyright holder. To view a copy of this licence, visit <http://creativecommons.org/licenses/by-nc-nd/4.0/>.

© The Author(s) 2025